Pump-probe method for measurement of thickness of molten layer produced by ultrashort laser pulse

N. A. Inogamov[*], V. V. Zhakhovsky[†], S. I. Ashitkov[**], M. B. Agranat[**], P. S. Komarov[**], V. A. Khokhlov[*] and V. V. Shepelev[‡]

[*] *Landau Institute for Theoretical Physics, RAS, Chernogolovka 142432, Russia*
[†] *Department of Physics, University of South Florida, Tampa, Florida 33620, USA*
[**] *Joint Institute for High Temperatures, RAS, Moscow 125412, Russia*
[‡] *Institute for Computer Aided Design, RAS, Moscow 123056, Russia*

Abstract. Pump-probe technique provides an unique method for high precision measurement of ultrafast processes induced in material by ultrashort laser pulses. The time domain and space domain available for measurements are 0.1–1000 ps and 1–1000 nm, respectively. In this respect the pump-probe technique noticeably extends to smaller scales the well-known Doppler Velocity Interferometer System for Any Reflector (VISAR) and Optically Recording Velocity Interferometer System (ORVIS) methods, which have micron-nanosecond accuracy. VISAR and ORVIS are widely used for study of wave dynamics in material plate having thickness from tens microns to several millimeters.

For the first time we apply pump-probe technique for deep probing of ultrasonic melting of micron-size aluminum film irradiated by ultrashort laser pump pulse. The pump with duration less than ~ 1 ps may result in ultra-high strain rate $\dot{V}/V \sim 10^9 - 10^{10}\,\mathrm{s}{-}1$ in such thin film. The experimental data and simulation analysis of material response and pressure wave dynamics are presented. The tensile strength of molten aluminum for different temperatures and strain rates was obtained.

Keywords: ultrashort laser-matter interaction, melting, molecular dynamics
PACS: 79.20.Eb, 61.43.Bn, 83.60.Uv, 47.61.-k

Ultrashort laser pulses (usLP) are widely used in the manufacturing technologies and for the study of ultrafast phenomena induced in various materials [1].

One of the most powerful technique important for experimental studies is the pump-probe interferometry [2, 3]. This is a way to determine the temporal evolution of surface displacement $\Delta x(t)$, where the light reflecting boundary of moving condensed phase remains atomically thin after a pump pulse with moderate fluence $F_{inc} \sim 1\,\mathrm{J/cm^2}$. We trace the sequence of events taking place inside the irradiated Aluminum film using our two-temperature (2T) hydrodynamic and large-scale molecular dynamic (MD) computer simulations and compare simulated data with the experimentally measured displacement $\Delta x(t)$ as a function of time.

Processes initiated by usLP in thin metal film deposited on thick glass substrate are investigated in the paper. The glass plate $-150\,\mathrm{microns} < x < 0$ with thickness of 150 microns shown in Fig. 1 is large in comparison with thickness d of Al film $0 < x < d$ deposited on to glass surface. The pump laser pulse arrives at normal incidence to the *left* boundary $x = 0$ of the Al film through transparent glass. Let's call the boundary

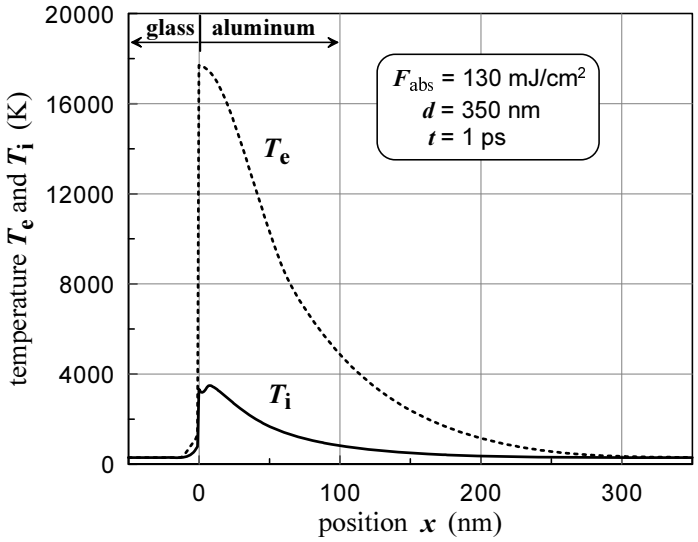

FIGURE 1. Distribution of electron and ion temperature after pump pulse. Before irradiation the glass-aluminum contact surface was at $x = 0$, where glass substrate has $x < 0$ and Al film $x > 0$.

between glass plate and Al film as a contact surface. In Fig. 1 a probe pulse arrives from the right side to the *right* boundary of the film, which is the rear-side boundary $x = d = 350$ nm with respect to the contact surface (frontal boundary) heated by pump pulse arriving from the left. The probe pulse is used to determine rear-side displacement $\Delta x(t) = x_{rear}(t) - d$ [2, 3], where the point $x = 0$ coincides with position of the unperturbed contact surface.

The problem of usLP absorbtion was solved by the use of 2T hydrodynamics code (2T-HD) in Lagrangian coordinates [3]. We use the same parameters as in experimental conditions; Ti:sapphire laser having pump and probe pulse duration $\tau_L = 90$ fs, absorbed fluence of pump $F_{abs} = 130\,\mathrm{mJ/cm^2}$, pump wavelength $\lambda_{pump} = 800$ nm, and probe wavelength $\lambda_{probe} = 400$ nm. The intensity of the pulse is represented by function $I(t) = I_{max}\exp(-t^2/\tau_L^2)$. Diameter of pump beam 82 microns is much larger than thickness $d_T \approx 100$ nm of the heat affected layer, and larger than thickness of deposited films lying from 350 to 1200 nm. Therefore, we may solve problem in one-dimensional approximation, where the hydrodynamics x-axis is normal to target surface. The wide-range equation of state of aluminum [5] and data from web cite [5] were used. Simulation results are presented in Figures 1 and 2. The main parameters describing 2T state are e-i energy exchange coefficient α and electron thermal conductivity κ_e. For Al the coefficient $\alpha \approx 3.6 \cdot 10^{18}\,\mathrm{erg/(\,s\,cm^3\,K)}$ is well known [6]. It is safe to assume that α is equal above constant since $\alpha(T_e)$ weakly depends on electron temperature.

Absorbtion of pump usLP leads to significant overheating of electron subsystem [3, 4], which results in decreasing of degree of electron degeneracy during usLP. In such conditions the time of electron-electron relaxation becomes short as $t_{ee} \sim 10$ fs. Then, there exits two-temperature (2T) state during period of $t_{ee} < t < t_{eq}$, since for moderate fluences of interest the electron-ion (e-i) relaxation time is $t_{eq} \sim 3 - 4$ ps. For the time shown in Fig. 1 the e-i relaxation is not yet completed. The heating layer

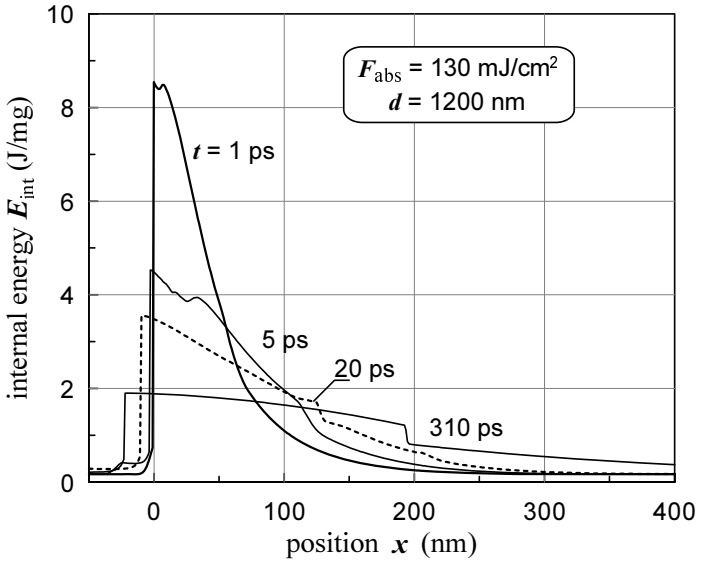

FIGURE 2. Redistribution of total internal energy $E_{int}(x,t)$ with time as a result of heat conduction with electron thermal conductivity κ_e in Al film. Lattice thermal conductivity was neglected in our calculations. The jump E_{int} at $x \approx 0$ is related to glass-Al contact surface. This surface moves gradually to the left due to higher pressure on Al side.

is mostly formed during the 2T stage, when electron heat propagates with supersonic speed into the bulk from skin layer of $\approx 15\,\text{nm}$ thick. For $t > t_{eq}$ heat front decelerates to subsonic regime, and the expansion of heated zone slows down substantially. Above-stated transition from fast to slow heat propagation stage is illustrated in Fig. 2, where the maximum of distribution $E_{int}(x,t)$ along x decreases by one half in the first several picoseconds. In order to drop by next half it requires hundreds picoseconds.

For given absorbed fluence F_{abs} the heating depth d_T and thickness of molten Al layer are determined by thermal conductivity κ_e, since, as stated above, the coefficient α is fixed. In calculation shown in Figures 1 and 2 the function $\kappa_e(T_e, T_i, \rho)$ was taken from the model [7], which presently provides the best agreement with experimental data in comparison with other models. As we show later the 2T-HD simulations with κ_e from [7] agree well with our experimental data. The amplitude and width of pressure wave depends on the heating depth. The greater is heating depth, the less amplitude of pressure and wider the pressure wave for given F_{abs}.

It is known [8] that, firstly, the fast heating by usLP results in sharp increase of pressure and formation of pressure waves moving from heated layer, secondly, the reflection of these waves from film boundaries leads to displacements of boundary positions. In this work the displacement of free rear side of film $\Delta x(t)$ is considered. It is necessary to note that the simulated wave profiles were obtained for Al film deposited on glass substrate, which qualitatively differs from waves in free-standing foil investigated [8]. In the last case foil has two free boundary contacting with air. Let's call free-standing material layer as a foil and layer deposited on substrate as a film.

The frontal side of film contacting with glass plate is irradiated by pump usLP. The formed sonic wave/perturbation interacts with frontal boundary. Because acoustic

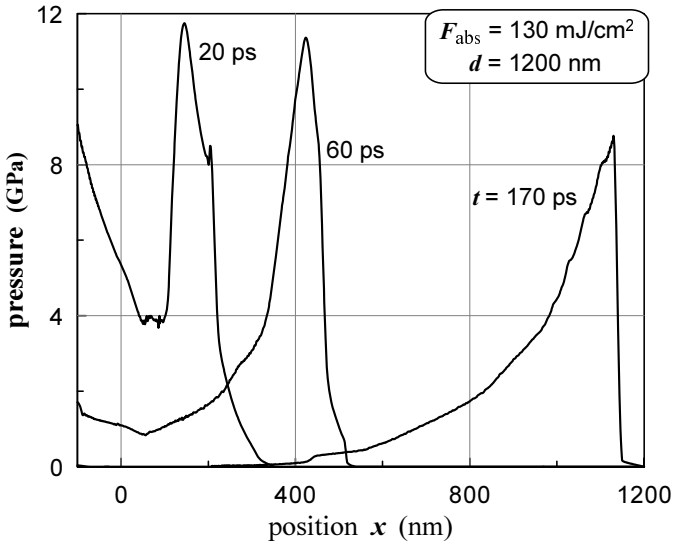

FIGURE 3. Compression wave p_+ leaves the heated layer d_T near contact surface $x \approx 0$, and it propagates toward rear-side boundary $x = d$. Shock wave in glass $x < 0$ is not shown, since we study evolution of wave p_+ within Al film.

impedance of contact between glass and Al is much different from that in contact air-Al, the wave-contact interactions will differ for films and foils. In the case of foil the compression wave $p > 0$ is followed by rarefaction wave $p < 0$ [8], while there is another wave picture for the case of film.

Let's compare the wave dynamics in foils in films. Figures 1 and 2 show right-moving waves $x > 0$ started from initial position of frontal boundary $x = 0$. In linear acoustic approximation, where sound speed c_s does not depend on amplitude of wave, these waves should have a form $p(x - c_s t)$. The leading parts of wave profile up to pressure maximum are identical in foils and films, if F_{abs} are equal. These parts do not "know" about frontal boundary conditions. Behind the maximum of pressure a rarefaction wave is formed. As we mentioned above for foils, there is a adiabatic stretching of metal below normal density under action of negative pressure $p < 0$. Whereas in films the maximum of pressure is followed by long "tail" having positive pressure. Such wave structure results in smaller stress appearing at rear side of film $x = d$ after wave reflection than it takes place in the case of foils. As a consequence, the spallation fluence threshold is higher for films.

Figure 3 shows the propagation of wave in a film. The wave is slightly nonlinear. Unlike linear acoustics, the characteristics converge on the leading part of wave profile with increasing pressure and diverge in lagging part with decreasing pressure. This is why the leading part breaks into shock wave, the maximal pressure decreases with time, and the lagging part becomes wider along the x-axis. In linear acoustics the wave profile propagates with standing shape $p(x - c_s t)$.

The response of rear-side surface to reflection of compression wave p_+ is presented in Fig. 4. In linear acoustic two functions $p(x - c_s t)$ and $u(t) = (d/dt)\Delta x(t)$ are similar under appropriate scaling of axes t and x. Al film shown in Fig. 4 has thickness

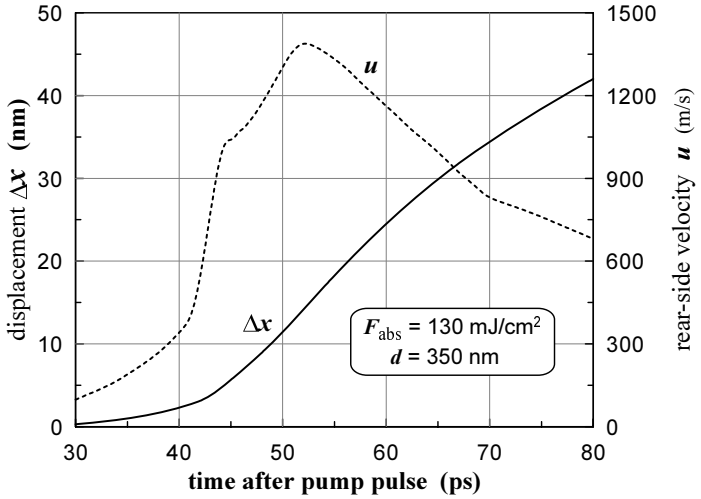

FIGURE 4. Displacement $\Delta x(t)$ and velocity $u(t)$ of rear side of film with thickness of $d = 350$ nm. Inflection of curve $\Delta x(t)$ corresponds to the maximal velocity.

$d = 350$ nm, while it is 1200 nm thick in Fig.3. Compression waves p_+, which leads to displacement $\Delta x(t)$, are almost equal on both Figures at the time $t = 20$ ps. This is why the pressure profile $p(x, t = 20\,\text{ps})$ in Fig. 3 and rear-side speed $u(t)$ in Fig. 4 are similar. For illustration of relations in chain of pump usLP $\rightarrow$ compression wave $p(x,t)$ $\rightarrow$ displacement $\Delta x(t)$ we study a film with smaller thickness, since the structure of wave $p(x,t)$ becomes simpler with propagation. Indeed, because of convergence of characteristics the leading part of wave ahead of shock decays with time, and the distance between shock and the maximal pressure decreases as well, see profiles in 3.

It is known [8, 9], that the compression wave p_+ having $p > 0$ transforms into rarefaction wave p_- with negative pressure $p < 0$ after reflection from free rear-side surface of film at $x = d$. The reflected wave p_- moves to the left toward the layer of molten metal as shown in Fig. 5. The curve "envelope“ follows through the maxima of tensile stresses of moving wave p_-. The amplitude of maximal stress gradually increases as the wave moves away from rear boundary, and saturates at some distance. The two factors define such behavior; first, the free boundary condition $p(x = x_{rear}(t), t) = 0$, and second, the finite width of the wave p_+ results in stress saturation at distance of the order of the wave width.

The wave with negative pressure p_- shown in Fig. 5, as well as the wave p_+ on Fig. 3, is moderately nonlinear wave – the effects of convergence and divergence of characteristics are considerable. The amplitude of pressure minimum on Fig. 5 slowly decreases after saturation point. The left part of the reflected wave becomes wider, while the right part steepens. One can note that the left part is a image of shock front on compression part of pressure wave p_+ and the right part represents the rarefaction part of this pressure wave. With time the right side of reflected wave p_- breaks into shock wave, see pressure profiles at 205 ps and 307 ps in Fig. 5. The pressure jump corresponds to Hugoniot adiabat started from negative pressure in stretched material. The shock moves faster than characteristics and it leads to reducing of pressure well

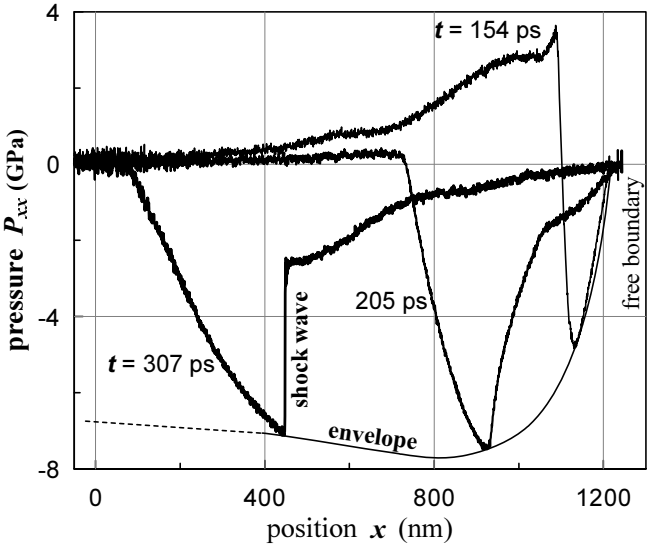

FIGURE 5. MD simulation of Al film with thickness $d = 1200\,\text{nm}$ irradiated by usLP with fluence $F_{abs} = 130\,\text{mJ/cm}^2$. Reflection of compression wave p_+ shown in 3 from rear side of film. The formation of reflected rarefaction wave p_- moving to the left is shown. "Envelope" follows through the maxima of tensile stresses of the reflected wave.

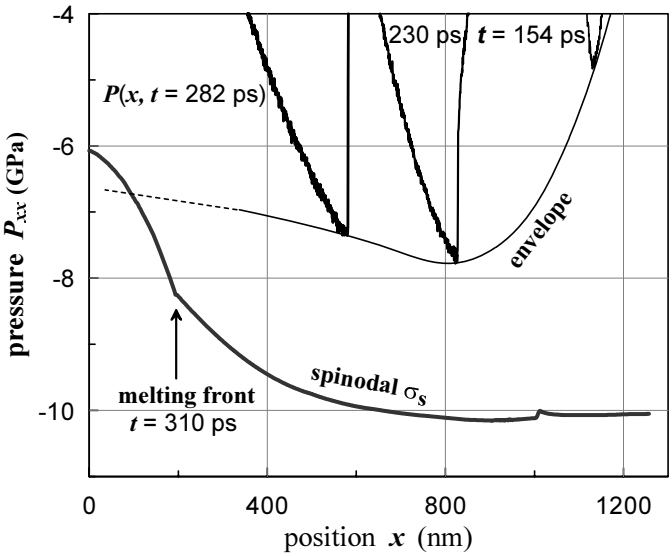

FIGURE 6. Relation between spinodal strength $\sigma_s(x)$ of nonuniformly heated Al film and "envelope" of wave $p(x,t)$ taken from Fig.5. The idea of probing of melting front is based on distinct difference of material strength in liquid and solid phases, and slow changes of tensile stress in moving rarefaction wave. The probing requires wave amplitudes to be between nucleation thresholds of melt and solid.

shown in Fig. 5

In linear acoustic the amplitude of wave p_- is proportional to the amplitude of p_+ after saturation. For strong enough wave p_+ the stress in reflected wave p_- may exceed the threshold equal to the material strength σ_s, and spallation of rear-side layer will

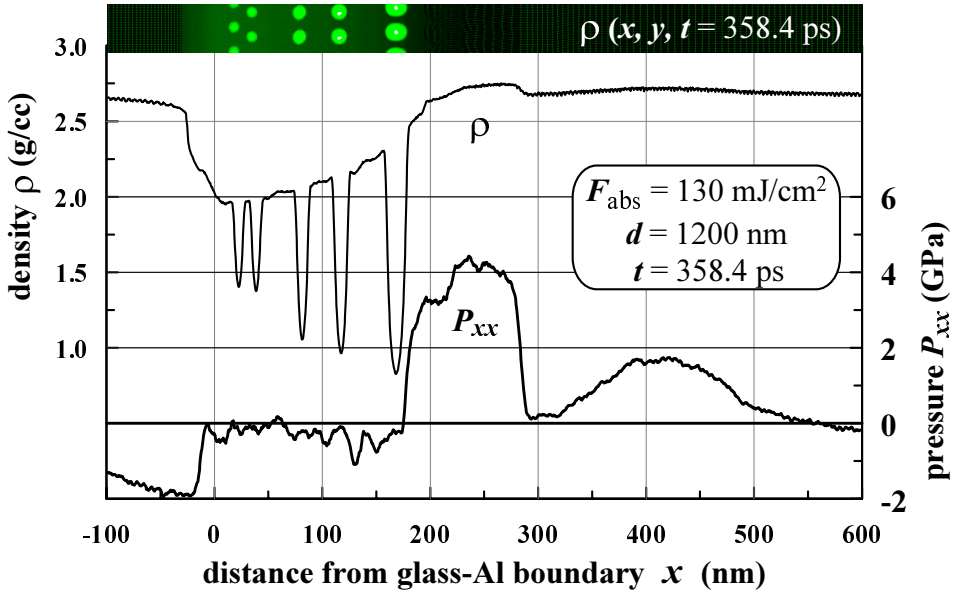

FIGURE 7. Cavitation in molten Al at $t = 359$ ps under strong tensile stress caused by coming wave p_-. The density profile $\rho(x)$ is obtained by collection of all atoms within small slab in plane $y-z$. Density gaps are related to large bubbles shown in density map $\rho(x,y)$ above the graph. The map was doubled in y-direction.

take place. The thickness of spalled layer d_{sp} at spallation threshold is determined by distance from rear surface to point where stress saturation occurs, see the minimum on "envelope" shown in Fig. 5.

The thickness d_{sp} decreases with increasing amplitude of wave p_+ if it exceeds the spallation threshold in material with constant strength independent from x. Spallation may also occur if the material strength $\sigma_s(x)$ is a function of coordinate. Such unusual condition is realized in the case of Al film heated through glass substrate. The hot layer of Al with thickness d_T is formed near glass-Al contact surface as shown in Fig. 2. It has the strength $\sigma_s(T)$ decreasing with temperature [9]. The estimate σ_s can be obtained with the help of spinodal line $p_{spin}(T)$, which can be taken from the wide-range equation of state [5, 10]. Then, let's take calculated temperature profile $T(x,t)$ from Fig. 2. The time when the reflected wave p_- arrives in molten layer is $t = 310$ ps as Fig. 6 indicates. Since the temperature profile $T(x,t)$ changes slowly for times longer $\sim 10^2$ ps, it can be written as a function of coordinate only $T(x)$. Finally, the stresses lying on spinodal $\sigma(x) = p_{spin}(T(x))$ can be calculated as a function of x. The curve $\sigma(x)$ marked as "spinodal" is shown in Fig. 6

One can compare "spinodal" and "envelope" functions in Fig. 6. It is clear that the stresses in reflected wave are not enough for spallation in cold solid, but they becomes stronger than "spinodal" stress within molten material. Such combination of material properties and wave configuration is unusual since spallation of solid is replaced by cavitation of melt and the thickness of spalled layer becomes anomalous large. Indeed, the maximal thickness of spalled layer d_{sp} is now determined by distance to molten layer, not by saturation point shown in Fig. 5. For the thick enough film this thickness

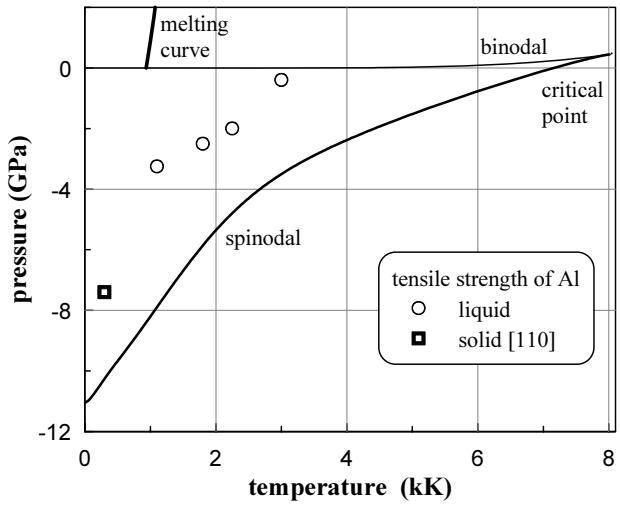

FIGURE 8. Tensile strength of solid and molten Al evaluated from MD simulations. Melting curve, binodal and spinodal lines taken from [5, 10, 11]

can be rather large.

MD simulation results of Al perfect crystal film at standard conditions $p = 0$ and $T = 300\,\mathrm{K}$ irradiated by usLP are presented in Figs. 5 and 6. Simulation set-up is the same as in [8]. The crystal axis [111] was oriented along the x-axis. The power $E_{ei}(x)$ gained by ions from hot electrons is calculated by 2T-HD code during short 2T stage. Then, this profile is used to simulate the heating of ions until t_{eq} in MD code. The advantage of MD approach consists in adequate description of metastable states with $p < 0$ and their decays, which is difficult to achieve in hydrodynamics modeling.

Figure 7 shows the density distribution/map after 10 ps of the beginning of cavitation in molten Al. In this case the amplitude of tensile wave exceeds the tensile strength everywhere in liquid Al. It results in cavitation of the entire molten layer. Notice that the dashed part of "envelope" line in Figs. 5 and 6 shows possible tensile stresses in the absence of nucleation of voids. In cavitation zone these stresses decline rapidly to zero. The tensile strength of molten Al and spall strength of solid Al, shown in Fig. 8, were determined from pressure profile just before first void/crack appears in its position on this profile. For the same moment the mass velocity profile was used to obtain local strain rate, since local $\dot{V}/V = dv_x(x)/dx$. For spallation of solid Al strain rate was $\dot{V}/V = 4.3 \cdot 10^9\,\mathrm{s}^{-1}$ [8], and for cavitation of melt four circles in Fig. 8 correspond to strain rate sequence $1.2; 1.9; 2; 1.5 \times 10^9\,\mathrm{s}^{-1}$ along increasing temperature.

The sharp drop of the stress in cavitation zone leads to formation of acoustic signal called as spallation pulse. The signal moves from cavitation zone to rear boundary of film. The arriving time of signal to rear boundary is shown by an up arrow in Fig. 9. The solid line presents the rear-side displacement obtained in MD simulation. Down arrow indicates the beginning time of nucleation in melt. The profile of acoustic signal is complicated by reflection from melting front. This profile is also affected by reflection of left-moving wave p_- from the melting front as well as wave refraction of right-moving spallation pulse.

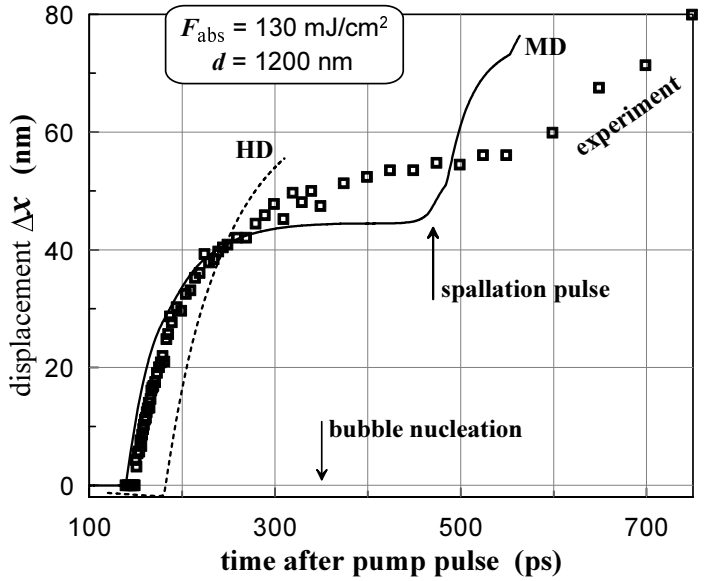

FIGURE 9. Comparison of experimental displacements (squares) with MD simulation (solid line) and 2T-HD calculation (dashed line) of rear side of Al film having thickness of 1200 nm.

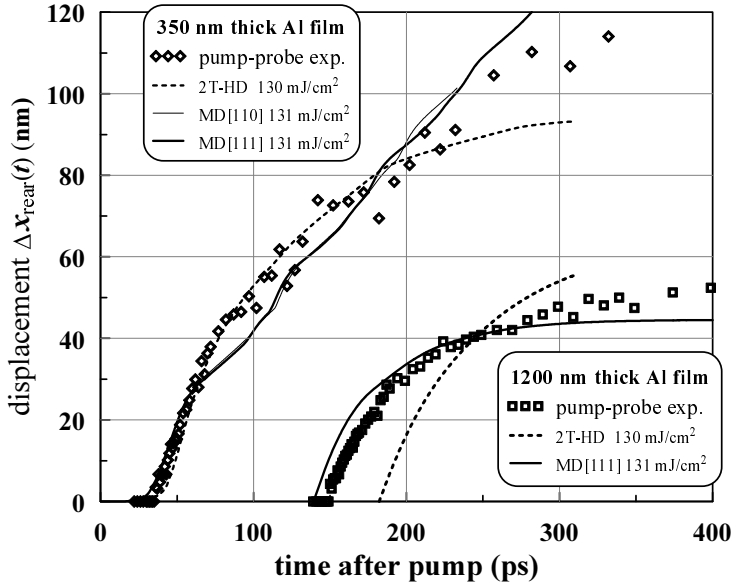

FIGURE 10. MD simulations are shown by solid lines, 2T-HD by dashed lines, symbols denote experimental data. For film thickness $d = 350$ nm MD gives nucleation moment $t = 82$ ps, the wave reflected from melting front comes to rear boundary at $t = 92$ ps, and spallation pulse arrives at $t = 110$ ps.

Comparison of simulation results with experimental data for two films with thicknesses 350 and 1200 nm is presented in Fig. 10. The energy of pump usLP $(64\,\mu\mathrm{J})$ and sizes of focal spots in experiments were identical. Similar experiments were done in work [12]. In our experiments the reference time was the same, but unfortunately the

arriving time of pump usLP to glass-Al contact surface is unknown. This is why the reference time for experimental data in Figs. 9 and 10 is shifted in such way, so early experimental displacement coincides with MD simulated displacement for Al film of $d = 350$ nm thickness.

Figure 10 clearly shows that 2T-HD simulated pressure wave p_+ moves slower than it is observed in MD simulations and experiments. The reason of this lies in smaller sound speed provided by wide-range equation of state, because Al crystal is described as a plastic solid which is valid only above dynamic yield stress σ_{el} [9] which substantially depends on strain rate $\dot{V}/V$. In area where stress is below this limit the crystal elasticity should be taken into account. The existing phenomenological elastic-plastic models predict the formation of elastic precursor ahead of plastic shock wave [9], but we do not observe plastic deformation and wave splitting in our MD simulations. We are planning to involve such models in our 2T-HD simulation in future.

From our simulation and experimental results we make up an unexpected conclusion - solid Al remains in elastic state at very high pressure exceeding σ_{el} by an order of magnitude. Plastic deformation in pressure wave p_+ does not occur since the high stress is applied during very short period of time ~ 30 ps.

In summary, we developed the method of acoustic probing of melting front position. The tensile strength of liquid Al was determined at very high strain rates. It is founded that 2T-HD modeling with the usage of ”plastic“ model of solid overestimates propagation time of pressure waves in Al film. We found that in crystal Al film the compression wave does not split in elastic precursor and plastic shock wave, and crystal remains in elastic state under action of very high but short pressure pulse.

ACKNOWLEDGMENTS

Authors from RAS are supported by RFBR grant No. 09-08-00969-a.

REFERENCES

1. C. Phipps (ed.), ’Laser Ablation and its Applications’, Springer Series in Optical Sciences, 129 (2007)
2. V.V. Temnov et al., J. Opt. Soc. Am. B **23**, No. 9, 1954 (2006).
3. N. A. Inogamov, V. V. Zhakhovskii, S. I. Ashitkov et al., Appl. Surf. Sci. **255,** 9712 (2009); arXiv:0812.2965v1[physics.optics].
4. S.I. Anisimov et al., Sov. Phys.-JETP **39,** 375 (1974).
5. A. V. Bushman, G. I. Kanel’, A. L. Ni, V. E. Fortov, *Intense dynamic loading of condensed matter,* Taylor & Francis Translation, 295 p. (1993). http://teos.ficp.ac.ru/rusbank/
6. Zh. Lin, L. V. Zhigilei, V. Celli, Phys. Rev. B **77,** 075133 (2008).
7. N. A. Inogamov, Yu. V. Petrov, JETP **110,** No. 3 (2010).
8. V.V. Zhakhovskii et al., Appl. Surf. Sci. **255,** 9592 (2009).
9. G. I. Kanel’, S. Razorenov, V. E. Fortov, *Shock-Wave Phenomena and the Properties of Condensed Matter,* Springer (2004).
10. M. E. Povarnitsin, P. R. Levashov, K. V. Khichshenko, *Physics of Extreme States of Matter - 2008,* Proc. of XXXIII Int. Conf. Equations of States of Matter, Eds. V.E. Fortov et al., El’brus, p. 161 (2008) [in Russian].
11. M.E. Povarnitsyn, K.V. Khishchenko, P.R. Levashov, Appl. Surf. Sci. **255,** 5120 (2009).
12. D.J. Funk, D.S. Moore, S.D. McGrane, K.T. Gahagan et al., Thin Solid Films **453-454,** 542 (2004).